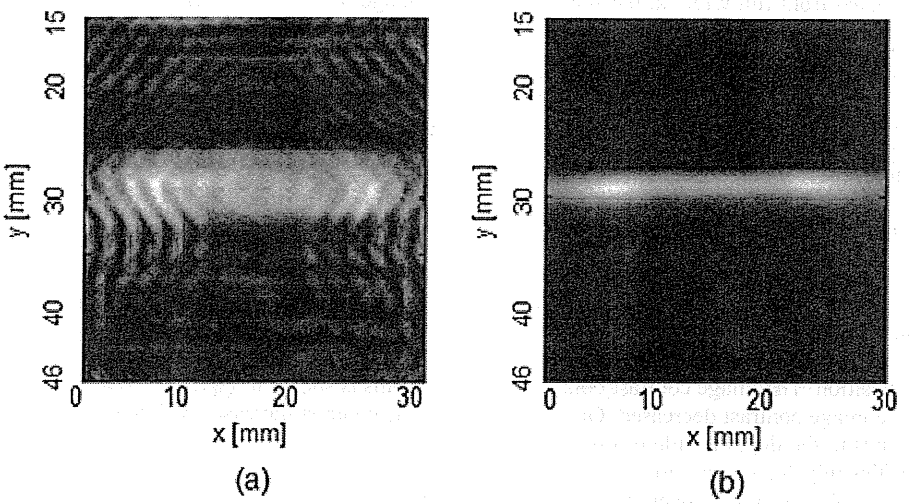

Figure 3. Reconstructed images (a) without and (b) with refraction correction.

3.2 Optical fluence distribution and lateral resolution

Figure 4(a) shows the log of normalized optical fluence calculated for the base phantom as a function of the imaging depth (z) when the dual illumination mode is used. The horizontal axis (z) represents the depth from the transducer surface excluding the holding plate. In this system, the incident laser energy density from backward illumination is set to be lower than that from forward illumination because it is necessary to reduce multireflection effect due to the holding plate of the surface-generated pressure wave on the reconstructed images. In the dual illumination mode, the optical fluence at the middle depth is lowest, which is useful for deep imaging.

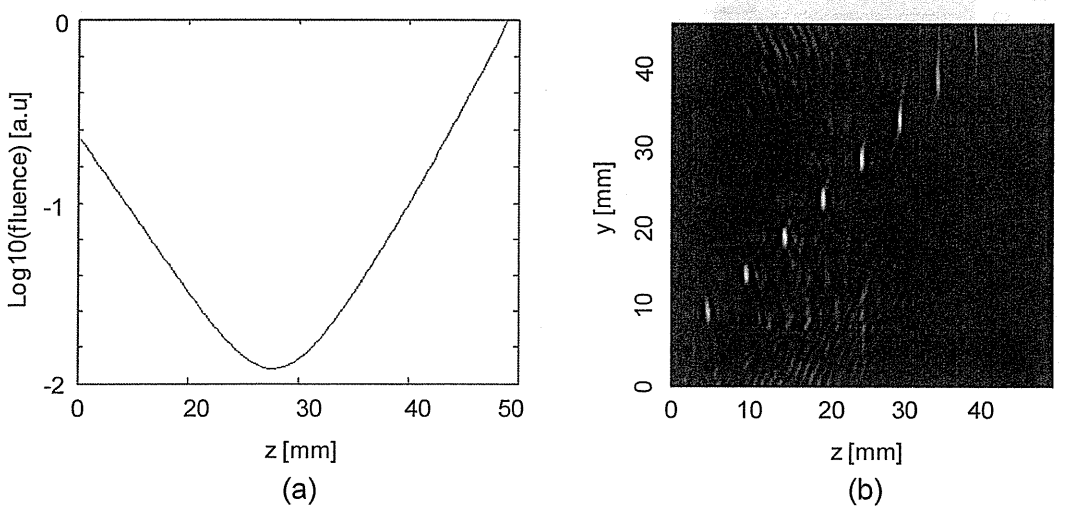

Figure 4. (a) Log of normalized optical fluence along the depth (z). (b) MIP image of the phantom for resolution evaluation.

Figure 4(b) shows the reconstructed images of the phantom for resolution evaluation. The image represents the maximum-intensity projection (MIP) of reconstructed volume through the x-z plane. To improve the image quality we averaged the PA signals 30 times. The thickness of the phantom was reduced to 48 mm by the gentle compression. All the absorbers embedded in the 50-mm-thick tissue-mimicking phantom were clearly imaged. Although the wire absorber at a depth of 45 mm was not imaged in Fig. 4(b), it could be imaged by changing the position of the phantom. The lateral

resolution was calculated from full width at half-maximum of the image profile. The lateral resolution remained near 2-mm within the first 20 mm of depth and then slowly widened to 3 mm at a depth of 45 mm. Theoretically, the lateral resolution is equal to the width of the detector element in terms of planar geometry [13]. Since the element size is 2×2-mm^2, a lateral resolution of 2 mm at a depth of the first 20 mm is consistent with the theory. Meanwhile, our PA simulation showed that the lateral resolution increased from 2 to 2.7 mm when the imaging depth increased from 10 to 40 mm, which is almost consistent with the experimental results. It is possible that the broadening of lateral resolution at a deep position is due to decreasing detection aperture.

3.3 Image contrast

Figure 5(a) shows a slice image of reconstructed volumes for the contrast evaluation phantom. A tube absorber at a 25-mm depth, where optical fluence along the depth is lowest as seen in Fig. 4(a), is shown. The result shows that the absorber at a 25-mm depth is well recognized. The image contrast at all depths was estimated from these slices. The image contrast was defined as the ratio of the average intensity at the 2-mm tube position and the average noise intensity of the outside tube position. The image contrast obtained from all depths is shown in Fig. 5(b). When the depth increased from 5 to 25 mm, the image contrast decreased. On the other hand, the contrast increases with a depth from 25 to 40 mm. This result corresponds to the depth profile of optical intensity in the system with dual illumination. Contrast of 4.1 at a 25-mm depth is sufficiently for recognition, as shown in Fig. 5(a). Therefore, the PAT system with dual illumination would have sufficient ability to image deeply located absorbers at a depth over 50 mm. The contrast at a 45-mm depth decreased from the 35-mm depth, which is due to artifacts from PA signals generated on the phantom surface.

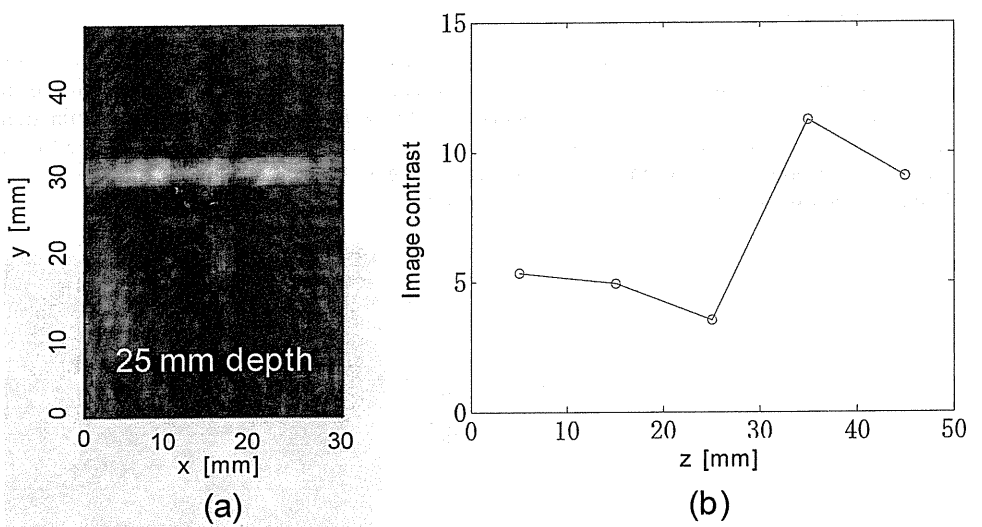

Figure 5. (a) Slice PA image of the 2-mm tube absorber at a depth of 25 mm. (b) Image contrast versus imaging depth (z).

4. CONCLUSION

We have characterized a new PAT system for deep tissue imaging. The PAT system simultaneously illuminates gently compressed tissues from a forward and backward direction toward an array transducer. The shape of the 345-element (15×23) transducer is rectangular, which allows direct illumination of tissue surfaces in front of the array transducer through a 10-mm-thick holding plate from the backward direction. The transducer frequency is designed at 1 MHz to receive PA signals from deep tissue with minimal ultrasonic attenuation. These system configurations make deep tissue imaging possible in terms of light penetration and ultrasound attenuation. System performance was tested in phantoms for lateral resolution and image contrast evaluation. The maximum incident laser energy density in this study was less than 10 mJ/cm^2, which is about 1/3 the ANSI safety limit at the wavelength of 797 nm. All absorbers of 10-dB contrast

embedded in the 50-mm-thick tissue-mimicking phantom were imaged with a lateral resolution of 2~3 mm. Since the light can reach deep tissues by the dual illumination, the PAT system enables diagnosis of breast cancers without hard compression.

ACKNOWLEDGEMENT

We acknowledge Yoshiko Wada, Takahiro Suita and Haruo Yoda for helpful discussions, and the team members of the Medical Imaging Project at Canon Inc. for the system development. We particularly thank Dr. Toshiyuki Kitai for helpful medical advices. This work is partly supported by the Innovative Techno-Hub for Integrated Medical Bio-imaging Project of the Special Coordination Funds for Promoting Science and Technology, from the Ministry of Education, Culture, Sports, Science and Technology, Japan.

REFERENCES

[1] American Cancer Society, [Breast Cancer Facts & Figures 2009-2010], American Cancer Society Inc., Atlanta & Georgia, 1-2 (2009).
[2] Li, C. and Wang, L. V., "Photoacoustic tomography and sensing in biomedicine," Phys. Med. Biol. 54, R59-R97 (2009).
[3] Manohar, S., Vaarjes, S. E., Van Hespen, J. C. G., Klaase J. M., Van den Engh, F. M., Steenbergen, W. and van Leeuwen, T. G., "Initial results of in vivo non-invasive cancer imaging in the human breast using near-infrared photoacoustics," Opt. Express 15(19), 12277-12285 (2007).
[4] Oraevsky, A. A., Karabutov, A. A., Solomatin, S. V., Savateeva, V., Andreev, V. G., Gatalica, Z., Singh, H. and Leming, R. D., "Laser optoacoustic imaging of breast cancer in vivo," Proc. SPIE 4256, 6-15 (2001).
[5] Song, K. H. and Wang, L. V., "Deep reflection-mode photoacoustic imaging of biological tissue," J. Bio. Opt. Let. 12(6), 060503 (2007).
[6] Ma, T., Kothapalli, S. R., Vaithilingam, S., Oralkan, O., Kamaya, A., Wygant, I. O., Zhunang, X., Gambhir, S. S., Jeffrey, R. B. and Khuri-Yakub, B. T., "3-D deep penetration photoacoustic imaging with a 2-D CMUT array," Proc. IEEE Ultrason. Symp., 5C-1 (2010).
[7] Ku, G. and Wang, L. V., "Deeply penetrating photoacoustic tomography in biological tissues enhanced with an optical contrast agent," Opt. Lett. 30(5), 507-509 (2005).
[8] Kim, C., Erpelding, T. N., Jankovic, L., Pashley, M. D. and Wang, L. V., "Deeply penetrating in vivo photoacoustic imaging using a clinical ultrasound array system," Biomed. Opt. Express 1(1), 278-284 (2010).
[9] Fukutani, K., Miyasato, T., Nakajima, T., Someda, Y., Asao, Y., Yagi, T., Yamakawa, M. and Shiina, T., "Dual illumination mode photoacoustic tomography for quantitative imaging," Proc. IEEE Ultrason. Symp., P5-M2-5 (2010).
[10] American National Standards Institute, [American National Standard for the Safe Use of Lasers Standard Z136.1-2007], American National Standards Institute, Washington, D.C., (2007).
[11] Xu, M. and Wang, L. V., "Universal back-projection algorithm for photoacoustic computed tomography," Phys. Rev. E 71, 016706 (2005).
[12] Tromberg, B. J., Shah, N., Lanning, R., Cerussi, A., Espinoza, J., Pham, T., Svaasand, L. and Butler, J., "Non-invasive in vivo characterization of breast tumors using photon migration spectroscopy," Neoplasia, 2(1-2), 26-40 (2000).
[13] Xu, M. and Wang, L. V., "Analytic explanation of spatial resolution related to bandwidth and detector aperture size in themoacoustic or photoacoustic reconstruction," Phys. Rev. E 37, 056605 (2003).

Proc. of SPIE. Vol. 7899, pp.78992G-1−78992G-8, 2010

Adaptive and Quantitative Reconstruction Algorithm for Photoacoustic Tomography

Shuhui Bu[a], Kengo Kondo[a], Makoto Yamakawa[b], Tsuyoshi Shiina[a], Kazuhiko Fukutani[c], Yasuhiro Someda[c], and Yasufumi Asao[c]

[a]Graduate School of Medicine, Kyoto University, 54 Shogoin-Kawaharacho, Sakyo-ku, Kyoto, Japan 606-8507;
[b]Advanced Biomedical Engineering Research Unit, Kyoto University, Kyoto, Japan;
[c]Medical Imaging Project, Canon Inc., 3-30-2 Shimomaruko, Ohta-ku, Tokyo, Japan 146-8501

ABSTRACT

Photoacoustic (PA) tomography is a rapidly developing imaging modality which can provide high contrast and spatial-resolution images of light absorption distribution in tissue. However, the quantitative reconstruction of absorption distribution is still a challenge. In this study, we propose an adaptive and quantitative reconstruction algorithm for reducing amplification of noises and artifacts in deep position due to light fluence compensation. In this method, the quantitative processing is integrated into the iterative reconstruction, and absorption coefficient distribution is iteratively updated. At each iteration step, the residual is calculated from detected PA signals and the signals calculated from a forward model by using the initial pressure which is calculated from the production of voxel value and the light fluence. By minimizing the residual, the reconstructed values are converged to the true absorption coefficient distributions. Since this method uses a global optimized compensation, better CNR can be obtained. The results of simulation and phantom experiment indicate that the proposed method provide better CNR at deep region. We expect that the capability of increasing imaging depth will broaden clinical applications.

Keywords: Photoacoustic tomography, model-based reconstruction, iterative reconstruction, quantitative reconstruction

1. INTRODUCTION

The PA effect[1,2] refers the generation of acoustic wave by the absorption of electromagnetic (EM) energy including optical and radio-frequency wave. In PA tomography (PAT), by illuminating the target with a short pulse laser, stress waves are produced because of the thermoelastic expansion. Acoustic sensors are placed at surrounding positions, and the PA signals are recorded. Through reconstruction algorithm, the absorption source can be recovered. Because the delivered energy type is light, the scatting of ultrasound echo imaging can be avoided. PAT combines the advantages of optical and acoustical methods: sensitive optical absorption contrast and low acoustic scatting in soft tissue. PAT has much better spatial resolution at depths exceed the optical ballistic regime than traditional optical modalities. Since the hemoglobin molecule of blood is the primary absorber in tissue, the absorbed optical energy distribution reconstructed by PAT can provides the local structure of blood circulation. In the early stage of cancer, the capillary vessel density is increased. Based on this fact, the cancer, especially breast cancer, would be detected by PAT.

One major problem in PAT is that the reconstructed information is not quantitative. Since tissue absorbs and scatters light, the optical fluence is decreased along light penetration depth. The pixels or voxels in reconstructed PAT images represent the level of absorbed optical energy, which is the product of the absorption coefficient and the optical fluence. Therefore, the CNR in the deep region of reconstructed image is low. Cox *et al.*[3] use a simple iterative method for quantitative reconstruction, but the fluence compensation is performed after image reconstruction. Since the CNR at deep region in the reconstructed images is low, amplification of the images also magnifies noises and artifacts, which decreases the image quality. Yuan *et al.*[4] proposed a quantitative

bushuhui@hs.med.kyoto-u.ac.jp; phone +81 75 751 4998

Photons Plus Ultrasound: Imaging and Sensing 2011, edited by Alexander A. Oraevsky, Lihong V. Wang,
Proc. of SPIE Vol. 7899, 78992G · © 2011 SPIE · CCC code: 1605-7422/11/$18 · doi: 10.1117/12.871436

reconstruction method by using diffusion equation based regularized Newton method. But in their method, the PAT images need to be segmented for getting prior structural information. Cox *et al.*[5] extended their work so that chromophore distribution can be estimated by using multi-wavelength excitation and gradient-based optimization techniques. Rosenthal *et al.*[6,7] using a sparse representation method for quantitative reconstruction, where the idea is based on the different spatial distribution properties of light fluence and absorption. Although in the method parameter-based fluence distribution is not needed, but under nonuniform boundary illumination, errors are occurred. Zemp *et al.*[8] proposed a method for quantitative reconstruction by using multiple optical sources even when the Grüneisen coefficient is spatially varying. However, in their method, reconstruction and transducer bandwidth must be ideal.

In this paper, we introduce an adaptive fluence compensation algorithm for 3-D planar PAT which can partly resolve the problem that amplification of noises and artifacts in deep region. An improved model-based (iterative) reconstruction algorithm is applied to ensure proper compensation for achieving quantitative reconstruction. Compared with conventional iterative reconstruction method,[9–11] the reconstructed image by this method is an absorption coefficient distribution. At each iteration step, the residual is calculated from detected PA signals and the signals calculated from a forward model by using the initial pressure which is calculated from the production of voxel value and the light fluence. By minimizing the residual, the reconstructed values are converged to the true absorption coefficient distributions. Because the light fluence compensation is combined in the reconstruction and a feedback is performed at each iteration, the amplification of noises and artifacts is less. The advantage of the proposed method is that reconstruction can be done under arbitrary illumination condition, less assumption is needed, and noises or artifacts at deep region of the reconstructed images are less. In addition, this method also inherits the advantages of iterative reconstruction method, such as less limited-view artifacts[9] and artifacts due to nonuniform sound speed.[12] The results of simulation and phantom experiment indicate that the proposed method performs better than conventional methods.

The rest of this paper is organized as follows. In section 2 we present the principle of the proposed method. The numerical simulation and phantom experiment are described in section 3. Finally, the conclusions of our work are provided in section 4.

2. METHOD

PA wave generated in an acoustically homogenous and non-viscous medium can be described as:[13,14]

$$\nabla^2 p(\mathbf{r},t) - \frac{1}{v_s^2}\frac{\partial^2}{\partial t^2}p(\mathbf{r},t) = -\frac{\beta}{C_p}\frac{\partial}{\partial t}H(\mathbf{r},t), \tag{1}$$

where $H(\mathbf{r},t)$ is heating function defined as the thermal energy converted at position $\mathbf{r}$ and time t by the EM radiation per unit volume per unit time, C_p is the isobaric specific heat, β is the isobaric volume expansion coefficient, and v_s is the acoustic speed.

The amount of generated heat in tissue is generally proportional to the strength of the input light intensity and absorption coefficient, and the definition is

$$H(\mathbf{r},t) = \mu_a(\mathbf{r})\Phi(\mathbf{r},t). \tag{2}$$

Here, μ_a is the absorption coefficient and Φ is optical fluence. Under both thermal and stress confinement conditions, heating time can be treated as a delta function, such as $H(\mathbf{r},t) \approx \mu_a(\mathbf{r})\Phi(\mathbf{r},t)\delta(t)$. The initial pressure p_0 of the absorber at position $\mathbf{r}$ can be calculated by

$$\begin{aligned} p_0(\mathbf{r}) &= \frac{v_s^2\beta}{C_p}\mu_a(\mathbf{r})\Phi(\mathbf{r},t) \\ &= \Gamma\mu_a(\mathbf{r})\Phi(\mathbf{r},t), \end{aligned} \tag{3}$$

where Γ is the Grüneisen coefficient expressed as $\Gamma = \beta v_s^2/C_p$. Here we assume Grüenisen coefficient is const in the region of interest (ROI).

The wave equation (1) can be solved by using a Green function approach.[1] Under the acoustic stress confinement, the heating process is treated approximately as a Dirac delta function, and the solution is:

$$p(\mathbf{r},t) = \frac{\beta}{4\pi C_p}\frac{\partial}{\partial t}vp, \tag{4}$$

$$vp = \int_V d\mathbf{r}' \frac{\mu_a(\mathbf{r})\Phi(\mathbf{r},t))}{|\mathbf{r}-\mathbf{r}'|}\delta\left(t-\frac{|\mathbf{r}-\mathbf{r}'|}{v_s}\right). \tag{5}$$

Above equations describe the relation that the detected PA pressure at position $\mathbf{r}$ and time t comes from sources over a spherical surface centered at $\mathbf{r}$ with the radius of $|\mathbf{r}-\mathbf{r}'|$. Based on the above equations, extract analytic reconstruction method such as universal back-projection (UBP)[15,16] derived a reconstruction equation for reconstructing the initial pressure distribution. To obtain the absorption coefficient distribution, the only way is to compensate the light fluence after reconstruction of the initial pressure distribution. But this process makes the noises and artifacts amplified, which produces low quality image.

In the proposed method, we separated the light fluence and absorption coefficient at each voxel position. And the absorption coefficients are estimated by the model-based method which is iteratively updated, while the light fluence is calculated by Monte Carol method.[17] Based on the solutions (4)-(5) the forward model for calculating PA signals can be expressed in matrix form as:

$$\mathbf{p} = \mathbf{A}\mathbf{\Phi}\boldsymbol{\mu}_a, \tag{6}$$

where, $\mathbf{A}$ denotes the system matrix which represents the geometry relationship between initial pressure and detected PA signals, and $\mathbf{p}$ is detected PA signals. The detail definition of $\mathbf{A}$ is:

$$A_{i,j} = \frac{A^{vp}_{i,j+1} - A^{vp}_{i,j-1}}{2\Delta t}, \tag{7}$$

where i is sensor's position index, j is the PA signal index, and Δt is the time interval between two sampling points, $A^{vp}_{i,j}$ represents the velocity potential item. In the 3-D planar scanning environment, the voxel size is usually much larger than the distance between two sampling point. Therefore, the pressure data are not continuous after finite difference calculation. This process induces large amplitude fluctuation which prevents high accuracy forward modeling. In this research, a Gaussian function is applied to interpolate the velocity potential data for keeping accuracy of pressure calculation. The definition of interpolated velocity potential item is:

$$\begin{aligned} A^{vp}_{i,j} &= \frac{\beta}{4\pi C_p}\frac{h_{i,j}}{R_{i,j}}, \\ R_{i,j} &= |\mathbf{r}_i - \mathbf{r}_j|, \\ h_{i,j} &= \begin{cases} \exp\left(\frac{-2(R_{i,j}-t_j v_s)^2}{\Delta^2}\right) : if|t_j - \frac{R_{i,j}}{v_s}| < \Delta/v_s, \\ 0 : else \end{cases} \end{aligned} \tag{8}$$

where Δ is distance between the central point of adjacent voxels.

After the interpolation processing, accurate forward modeling can be achieved. However, the matrix $\mathbf{A}$ is very large, and it is also a sparse matrix that above 99% items are zero. By using the compressed sparse row (CSR) format,[20] the required memory can be greatly reduced. In the CSR format, only column indices, values and indices of nonzero items are stored. In PAT mode, the ultrasound sensors are assumed to receive pressure wave in the direction of $0 \sim 90$ degrees with same sensitive. But in real situation, the sensitivity is not uniform. In the far field, with the incident angle increasing the sensitivity is decreased. For compressing the matrix size of $\mathbf{A}$, if the incident angle is larger than a given threshold, its value is set to be zero so that the item is not stored. Based on the fact, the matrix $\mathbf{A}$ can be further decreased to about its half. The matrix can also be further compressed to its one-fourth based on the symmetry property of wave propagation property.[18] In total, the occupied memory can be approximately decreased to its 1/250 by using all above techniques.

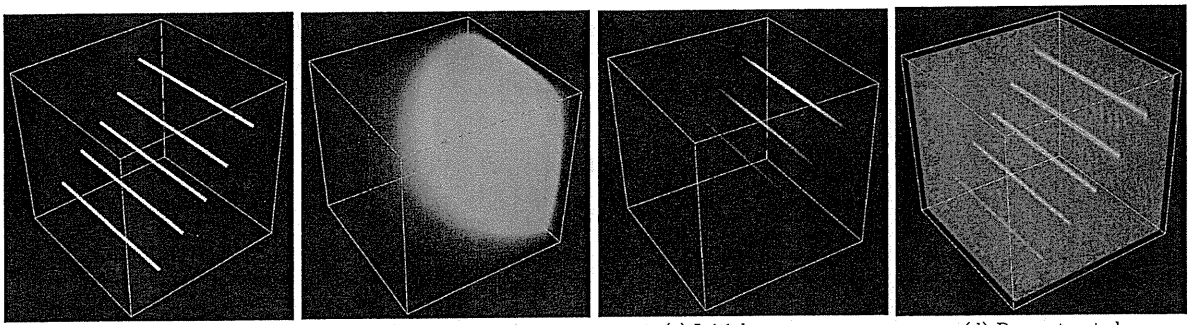

(a) Simulation model (b) Light fluence (c) Initial pressure (d) Reconstructed

Figure 1. (a) Numerical simulation model, (b) light fluence distribution calculated by Monte Carol method, (c) initial pressure distribution, and (d) quantitative reconstructed results by proposed method.

Table 1. Simulation parameters

Parameter name	Value
Sound speed	1500 m/s
Sampling frequency	20 MHz
Sampling point number	750
Sensor number in x and y axes	16
Sensor pitch in x and y axes	2.0 mm
Voxel number in x, y, and z axes	64
Voxel size in x, y, and z axes	0.5 mm

The quantitative absorption coefficient distribution is estimated by minimizing l_2 norm between detected signals and the PA signals calculated by the forward model, as shown:

$$\boldsymbol{\mu}_a' = \arg\min_{\boldsymbol{\mu}_a} ||\mathbf{p_d} - \mathbf{A}\Phi\boldsymbol{\mu}_a||_2. \tag{9}$$

Here, $\mathbf{p_d}$ is detected PA signals, and $\boldsymbol{\mu}_a'$ is optimal estimated absorption coefficient distribution. Conjugate gradient method is used to find the optimal estimation.

3. SIMULATION AND PHANTOM EXPERIMENTS

Proposed method was evaluated by numerically simulating a hypothetical model, as illustrated in Figs. 1(a)-(c). In this model, five rubber wires with a diameter of 0.5 mm were simulated. The background's absorption coefficient and reduced scattering coefficient were $\mu_a = 0.0078$ mm^{-1} and $\mu_s' = 0.9306$ mm^{-1}, respectively. A forward illumination (forward direction toward probe) was used, and the incident light pattern is shown in Fig. 3(b). The light fluence was calculated by Monte Carol method. The PA waves were simulated by using equations (4) and (5), and -30 dB white noises were added. The simulation parameters are summarized in table 1. After we obtained the simulated PA signals, a parallel implemented program was used to reconstruct the absorption coefficient distribution. Figs. 2(a1)-(a3) and (b1)-(b3) show the maximum intensity projection (MIP) images of absorption coefficient distribution and absorbed optical energy distribution, respectively. The resulting MIP images reconstructed by UBP with fluence compensation after reconstruction are shown in Figs. 2(c1)-(c3). The images reconstructed by proposed method are shown in Figs. 2(d1)-(d3). From the images, we can see that noises and artifacts are amplified at low fluence region in the images reconstructed by UBP with fluence compensation. In contrast, they are greatly decreased by using proposed method. In addition, although the target size in the images reconstructed by UBP is larger than actual size, the target size in images reconstructed by the proposed method is the same as actual size. This improvement is due to advantages of iterative reconstruction.

The performances were also tested by a tissue-mimicking phantom with embedded absorbers as shown in Fig. 3(e). The base of the tissue-mimicking phantom with a size of 70 (x) × 120 (y) × 50 (z) mm^3 was made with

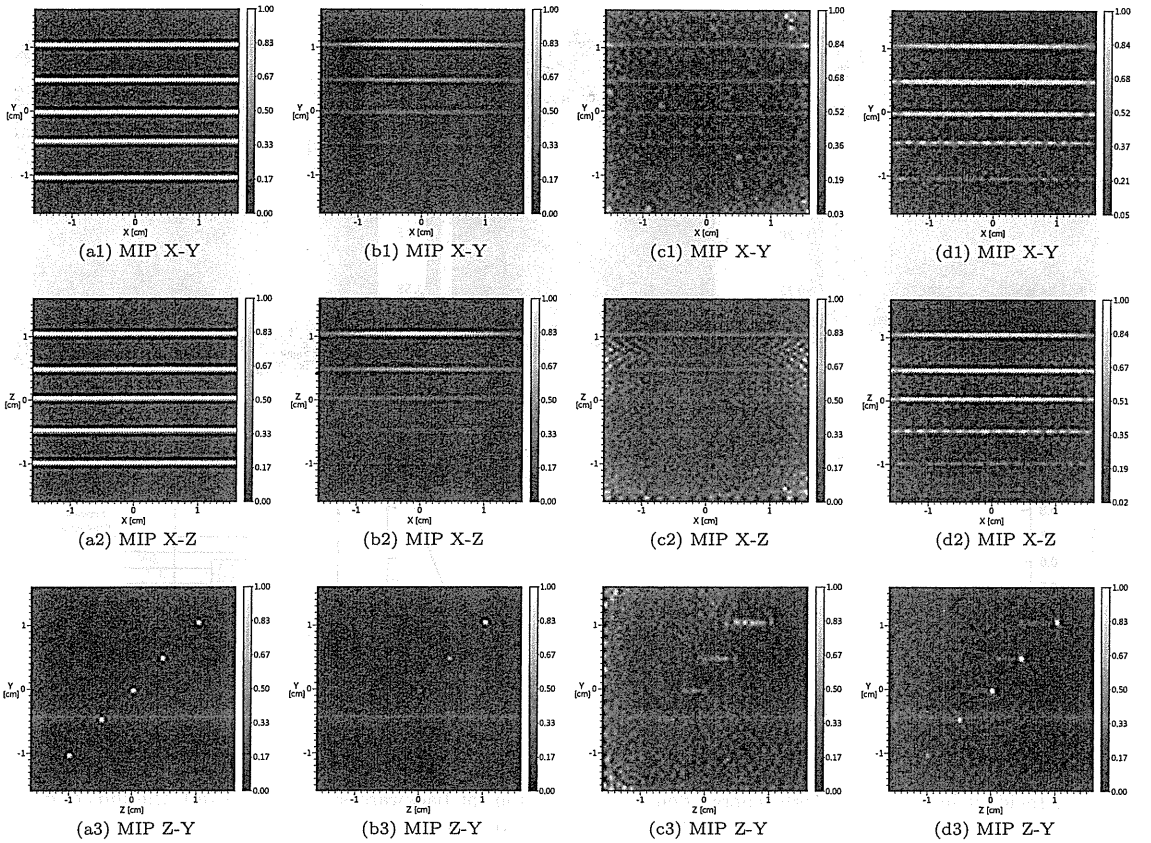

Figure 2. Simulation model and reconstructed images by conventional quantitative reconstruction method, and resulting images by proposed method. MIP X-Y is projection along Z axis, MIP X-Z is project along Y axis, and MIP Z-Y is projection along X axis. (a1)-(a3) Simulation model. (b1)-(b3) initial pressure distribution. (c1)-(c3) resulting images reconstructed by conventional quantitative reconstruction method. (d1)-(d3) resulting images reconstructed by proposed method.

urethane gel and curing agent. The absorption and reduced scattering coefficients of the base phantom were 0.0078 and 0.9306 mm^{-1} at the wavelengths of 797 nm, respectively. The sound speed of the base phantom was 1391 m/s. The rubber wires with diameter of 0.3 mm were embedded at depth of 5, 10, 15, 20, 25, 30, 35, 40 and 45 mm in the base phantom.

In the phantom experiment, a PA imaging system with dual illumination[19] was used. In the imaging system, the laser is dual illuminated to the target, therefore it is possible to image deep tissues. A system configuration of the system is described in detail elsewhere.[19] Briefly, two sets of a Ti:Sa laser (LT-2211, LOTIS TII) pumped by Q-swtich Nd:YAG laser (LS-2137, LOTIS TII) were used as the excitation source to provide 15 ns laser pulses with a 10 Hz pulse repetition rate. One was used for backward illumination (probe side), and another for forward direction (opposite side from probe) as illustrated in Fig. 3(e). In this experiment, a wavelength of 797 nm was used. The maximum incident light energy densities from backward and forward illumination on the sample surface were 3.11 and 9.46 mJ/cm^2, respectively. The distributions of incident light energy density are shown in Figs. 3(a)-(b), and the unit of colorbar is mJ/cm^2. The light fluence was calculated by Monte Carol method, as shown in Fig. 3(c). The profile of light fluence at center of the probe along the depth is shown in Fig. 3(d). A 2-D matrix probe was used to acquire PA signals. The central frequency of the probe is 1 MHz with an 80% bandwidth. The pitch of the sensor in both axes was 2 mm, and channel number in x and y axis

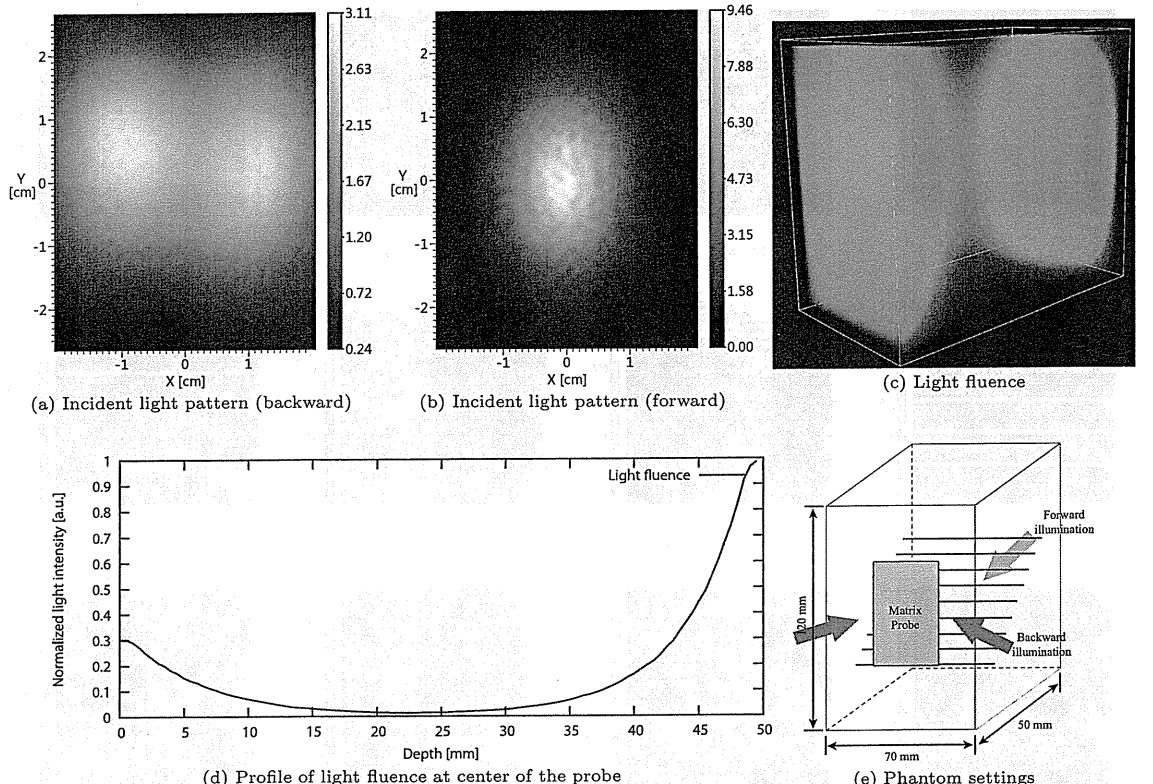

(a) Incident light pattern (backward) (b) Incident light pattern (forward) (c) Light fluence

(d) Profile of light fluence at center of the probe (e) Phantom settings

Figure 3. (a) Incident light pattern (light energy density distribution) at backward side (probe side), the unit of colorbar is mJ/cm^2. (b) Incident light pattern at forward side (opposite side from probe), the unit of colorbar is mJ/cm^2. (c) Light fluence calculated Monte Carlo method. (d) Profile of light fluence at center of probe. (e) Phantom settings and light illumination settings.

were 15 and 23, respectively. The sampling frequency was 20 MHz, and sampling point number was 1280. In the reconstruction, the voxel size was set to be 0.5 mm in all axes.

The resulting images are shown in Fig. 4. Figs. 4(a1)-(a3) and (b1)-(b3) show the MIP images reconstructed by UBP method without fluence compensation and with light fluence compensation, respectively. The MIP images reconstructed by proposed method are shown in Figs. 4(c1)-(c3). From the resulting images, we can see that the artifacts in the image reconstructed by the proposed method are greatly decreased compared with that reconstructed by conventional fluence compensation method. Because the light fluence at depth 25 mm is low, the wire target at the depth of 25 mm in the UBP reconstructed images can hardly be seen. After light fluence compensation, the resulting images reconstructed by conventional fluence compensation method amplify the artifacts and noises. In the proposed method, the compensation is done in each iteration which can make the overall noises and artifacts minimized. Therefore, in the resulting images of proposed method, the amplification of the noises and artifacts are less.

Proposed method can output better quality images which have fewer noises and artifacts, but two major problems need to be resolved before practical application. Firstly, proposed method need huge memory, and long calculation time. Compressed sensing reconstruction which can reduce measurement data will help to reduce the memory requirement. The calculation has potential of high performance parallel computation, therefore, in the following research GPU accelerated compressed sensing reconstruction method will be studied. Secondly, the iteratively reconstruction is more sensitive to noise compared with other methods such as UBP. More effective de-noising method and incorporation of noise modeling into the forward model will also be studied.

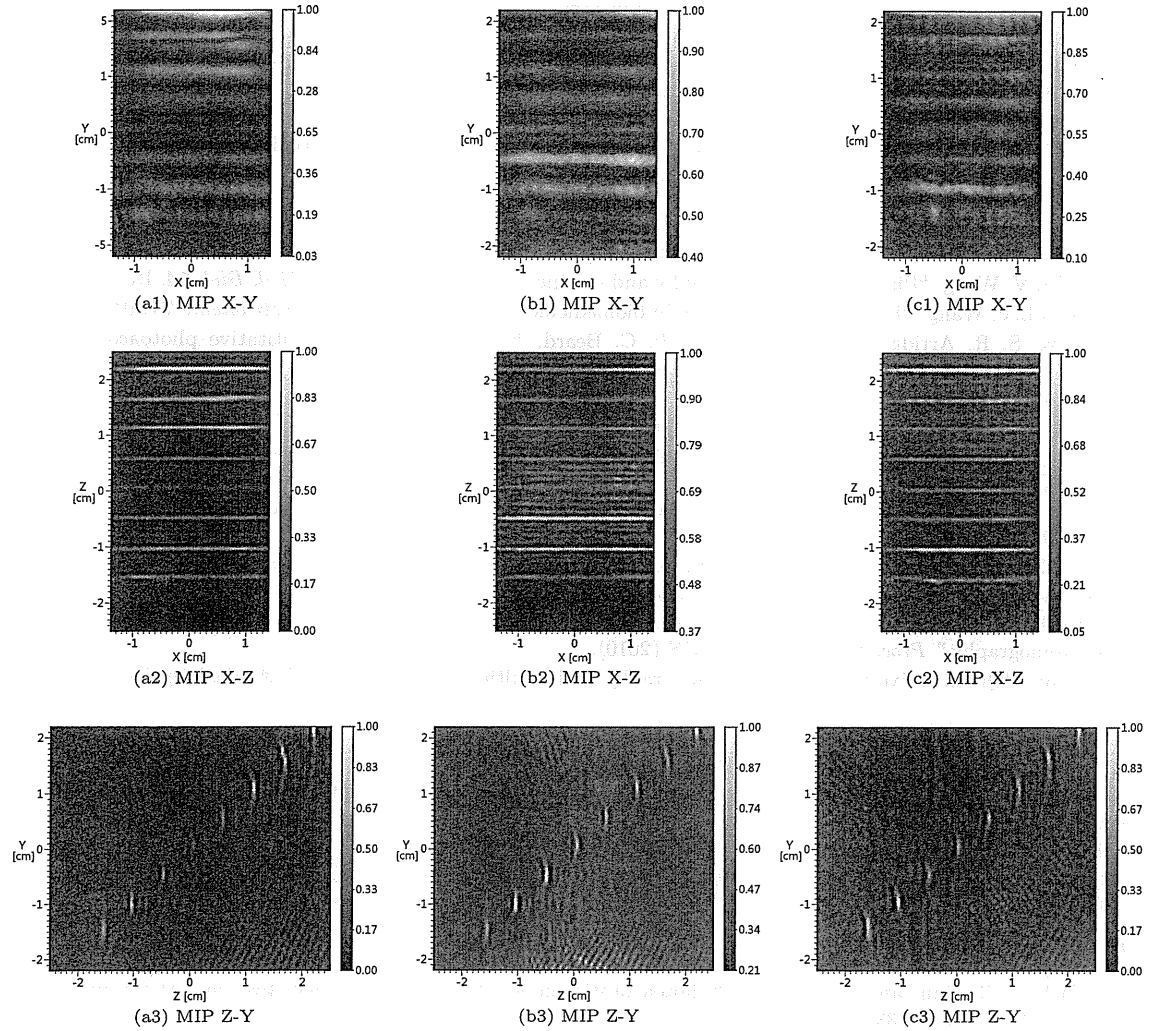

Figure 4. Reconstructed images by UBP method without fluence compensation, UBP with fluence compensation, and proposed method. (a1)-(a3) Reconstructed by UBP method without fluence compensation. (b1)-(b3) Reconstructed by UBP method with conventional fluence compensation. (c1)-(c3) Reconstructed by proposed method.

4. CONCLUSION

In this paper, we presented an adaptive and quantitative reconstruction method for 3-D planar PAT. The light fluence compensation is performed at each iteration, which can make the noise and amplification of artifacts minimized. In addition, matrix compress techniques make the proposed method applicable for 3-D planar scanning conditions, and the calculation speed is also accelerated. The simulation and phantom experiment results indicate that the proposed method reconstructs better quality images. We expect that the capability of increasing imaging depth will broaden clinical applications of PAT.

ACKNOWLEDGMENTS

The authors would like to acknowledge Takao Nakajima and Ryuichi Nanaumi for helping to evaluate the optical properties of the phantom, and the team members of the Medical Imaging Project in Canon Inc. for the PA imaging system development. This work is partly supported by the Innovative Techno-Hub for Integrated Medical Bio-imaging Project of the Special Coordination Funds for Promoting Science and Technology, from the Ministry of Education, Culture, Sports, Science and Technology, Japan.

REFERENCES

[1] C. Li and L.V. Wang, "Photoacoustic tomography and sensing in biomedicine," *Phys. Med. Biol.* **54**, R59-R97 (2009).

[2] M. Xu and L.V. Wang, "Photoacoustic imaging in biomedicine," *Review of Scientific Instruments* **77**, 041101 (2006).

[3] B. T. Cox, S. R. Arridge, K. P. Kostli, and P. C. Beard, "Two-dimensional quantitative photoacoustic image reconstruction of absorption distribution in scattering media by use of a simple iterative method," *Applied Optics* **45**(8), 1866-1875 (2006).

[4] Z. Yuan, Q. Wang, H. Jiang, "Reconstruction of optical absorption coefficient maps of heterogeneous media by photoacoustic tomography coupled with diffusion equation based regularized Newton method," *Optics Express* **15**(26), 18076 (2007).

[5] B.T. Cox, S.R. Arridge, and P.C. Beard, "Estimating chromophore distribution from multiwavelength photoacoustic images," *J. Opt. Soc. Am.* **26**(2), 443 (2009).

[6] A. Rosenthal, D. Razansky, and V. Ntziachristos, "Quantitative optoacoustic signal extraction using sparse signal representation," *IEEE Trans. Med. Imag.* **28**(12), 1997-2006 (2009).

[7] A. Rosenthal, D. Razansky, and V. Ntziachristos, "Sparse signal representation at the service of quantitative optoacoustic tomography," *Proc. SPIE* **7564**, 75640S (2010).

[8] R. J. Zemp, "Quantitative photoacoustic tomography with multiple optical sources," *Applied Optics* **49**(18), 3566 (2010).

[9] G. Paltauf, J.A. Viator, S.A. Prahl, and S.L. Jacques, "Iterative reconstruction algorithm for optoacoustic imaging," *J. Acoust. Soc. Am.* **112**(4), 1536-1544 (2002).

[10] J. Zhang, M.A. Anastasio, P.J.L. Riviere, and L.V. Wang, "Effects of different imaging models on least-squares image reconstruction accuracy in photoacoustic tomography," *IEEE. Trans. Med. Imag.* **28**(11), 1781-1790 (2009).

[11] S. Ma, S. Yang, and H. Guo, "Limited-view photoacoustic imaging based on linear-array detection and filtered mean-backprojection-iterative reconstruction," *J. Appl. Phy.* **106**, 123104 (2009).

[12] Z. Jing, W. Kun, Y. Yongyi, A.A. Mark, "Simultaneous reconstruction of speed-of-sound and optical absorption properties in photoacoustic tomography via a time-domain iterative algorithm," *Proc. SPIE* **6856**, 68561 (2008).

[13] P. M. Morse, and K. U. Ingard, "Theoretical acoustics," Princeton University Press, Princeton, NJ, (1987).

[14] G. J. Diebold, T. Sun, and M. I. Khan, "Photoacoustic monopole radiation in one, two, and three dimensions," *Phys. Rev. Lett.* **67**(24), 3384-3387 (1991)

[15] M. Xu and L.V. Wang, "Universal back-projection algorithm for photoacoustic computed tomography," *Physical Review E* **71**, 016706, (2005).

[16] M. Xu, Y. Xu, and L.V. Wang, "Time-domain reconstruction algorithms and numerical simulation for thermoacoustic tomography in various geometries," *IEEE. Trans. Bio. Eng.* **50**(9), 1086-1099 (2003).

[17] L.H. Wang, S. L. Jacques, and L.Q. Zheng, "MCML - Monte Carlo modeling of photon transport in multi-layered tissues," *Computer Methods and Programs in Biomedicine* **47**, 131-146 (1995)

[18] K. Tanji, K. Watanabe, K. Fukutani, Y. Asao, T. Yagi, M. Yamakawa, T. Shiina, "Advanced model-based reconstruction algorithm for practical three-dimensional photoacoustic imaging," *Proc. SPIE* **7899**, 7899-92 (2011).

[19] K. Fukutani, Y. Someda, M. Taku, Y. Asao, S. Kobayashi, T. Yagi, M. Yamakawa, T. Shiina, T. Sugie, and M. Toi, "Characterization of photoacoustic tomography system with dual illumination modes," *Proc. SPIE* **7899**, 7899-91 (2011).

[20] E. F. D. Azevedo, M. R. Fahey, and R. T. Mills, "Vectorized sparse matrix multiply for compressed row storage format," *Computational Science - ICCS 2005* **3514**, 99-106 (2005).

Proc. of SPIE. Vol. 7899, pp. 78992K-1－78992K-6, 2010

Advanced model-based reconstruction algorithm for practical three-dimensional photoacoustic imaging

Koichi Tanji*[a], Katsuhiro Watanabe[a], Kazuhiko Fukutani[a], Yasufumi Asao[a, c], Takayuki Yagi[a]
Makoto Yamakawa[b], Tsuyoshi Shiina[c]
[a]Corporate R&D Headquarters, Canon Inc., 3-30-2 Shimomaruko, Ohta-ku, Tokyo 146-8501, Japan
[b]Advanced Biomedical Engineering Research Unit, Kyoto University, Kyoto, Japan
[c]Graduate School of Medicine, Kyoto University, 54 Shogoin-Kawaharacho, Sakyo-ku, Kyoto 606-8507, Japan

ABSTRACT

In this study, we propose an advanced model-based reconstruction algorithm for three-dimensional photoacoustic imaging. The algorithm is based on accurate forward photoacoustic models and an optimization algorithm which minimizes the square of the error between the measured acoustic signals and the signals predicted by the forward models. The forward photoacoustic models incorporate system-configuration and detector-dependent factors such as frequency response and finite size effect. A conjugate gradient-based optimization algorithm is used for reconstructing images. In addition, we make use of the symmetry and locality of the photoacoustic waves in the computations of the forward photoacoustic models in order to reduce the memory requirements and computation time in three-dimensional image reconstruction. The results show that the proposed algorithm provides high-resolution and high-quality photoacoustic images.

Keywords: Photoacoustic imaging, forward model, model-based reconstruction, three-dimensional reconstruction

1. INTRODUCTION

Photoacoustic imaging (PAI) is a promising imaging modality, which can visualize biological tissues with high optical contrast and high spatial resolution. PAI has been used to visualize blood vessels, detect breast tumors, and estimate oxygenation levels. In order to reconstruct these images, conventional back-projection algorithms and Fourier transform algorithms [1][2] are widely used for PAI in spite of leading streak artifacts and blurring images when incomplete projection data are applied.

Although various model-based reconstruction algorithms [3][4][5] have been proposed to resolve these drawbacks, the application of such algorithms to three-dimensional PAI is restricted to small sizes or finite bandwidth due to large computational cost.

This work explores the possible application of a three-dimensional model-based reconstruction algorithm in the time domain. The algorithm incorporates system-configuration and detector-dependent factors such as frequency response and finite size effect as forward models, and solves the regularized normal equation to minimize an objective function. The objective function consists of the residual between the measured acoustic signals and the signals predicted by the forward models and the regularization term. We make use of the symmetry and locality of the photoacoustic waves in these computations so as to reduce the memory requirements and computation time in three-dimensional reconstruction.

We investigated the performance of the algorithm on numerical data in three-dimensional PAI. The results showed that the algorithm provides high-resolution and high-quality photoacoustic images which do not suffer from back-projection-related reconstruction artifacts or detector-related blur effect. In addition, the memory requirements and computation time of the three-dimensional reconstruction are significantly reduced, thus greatly increasing the possible reconstruction size.

*tanji.koichi@canon.co.jp; phone +81 3 3758 2111; fax +81 3 3757 3096

Photons Plus Ultrasound: Imaging and Sensing 2011, edited by Alexander A. Oraevsky, Lihong V. Wang,
Proc. of SPIE Vol. 7899, 78992K · © 2011 SPIE · CCC code: 1605-7422/11/$18 · doi: 10.1117/12.873704

2. THREE-DIMENSIONAL MODEL-BASED ALGORITHM

2.1 PAT system model

The system configuration of our developed photoacoustic tomography (PAT) system is described in detail elsewhere [6]. A schematic diagram of the PAT system is shown in Fig. 1(a). The system consists of two regions which have different sound speeds: one is a tissue region (the speed of sound is approximately 1500 m/s) and the other is a holding plate region (the speed of sound is typically 2200 m/s). A two-dimensional transducer array is in contact with the holding plate, and measures photoacoustic waves refracted by the interface. Each detector element of the array has a frequency response and finite-size effect.

Figure 1(b) shows the spatiotemporal variation of photoacoustic waves measured with the array. In the spatiotemporal space, the trajectories of photoacoustic waves describe quadric surfaces. The measured photoacoustic signals are used for image reconstruction.

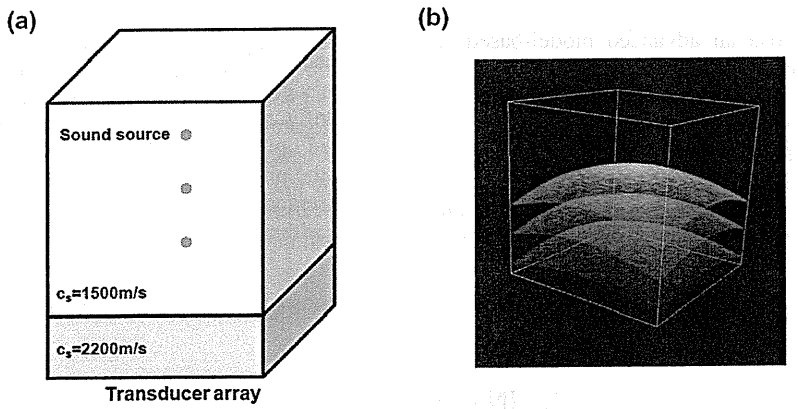

Figure 1. Illustration of (a) PAT system and (b) measured photoacoustic wave data.

2.2 Statistical optimization

In order to reconstruct images from the data obtained from the PAT system, a three-dimensional model-based algorithm is introduced. The sound waves are assumed to be linear in our model, and consequently sound waves from arbitrary sound sources are generated by the linear combination of sound waves which correspond to unit sources (Eq. (1)):

$$\mathbf{JP_I} \approx \mathbf{P_M} \tag{1}$$

$$\mathbf{J} = \begin{bmatrix} \frac{\partial P_{C[0][0][0]}}{\partial P_{I[0][0][0]}} & \frac{\partial P_{C[0][0][0]}}{\partial P_{I[0][0][1]}} & \cdots & \frac{\partial P_{C[0][0][0]}}{\partial P_{I[0][0][nz-1]}} & \cdots & \frac{\partial P_{C[0][0][0]}}{\partial P_{I[nx-1][ny-1][nz-1]}} \\ \frac{\partial P_{C[0][0][1]}}{\partial P_{I[0][0][0]}} & \frac{\partial P_{C[0][0][1]}}{\partial P_{I[0][0][1]}} & \cdots & \frac{\partial P_{C[0][0][1]}}{\partial P_{I[0][0][nz-1]}} & \cdots & \frac{\partial P_{C[0][0][1]}}{\partial P_{I[nx-1][ny-1][nz-1]}} \\ \vdots & \vdots & \ddots & \vdots & \ddots & \vdots \\ \frac{\partial P_{C[0][0][nt-1]}}{\partial P_{I[0][0][0]}} & \frac{\partial P_{C[0][0][nt-1]}}{\partial P_{I[0][0][1]}} & \cdots & \frac{\partial P_{C[0][0][nt-1]}}{\partial P_{I[0][0][nz-1]}} & \cdots & \frac{\partial P_{C[0][0][nt-1]}}{\partial P_{I[nx-1][ny-1][nz-1]}} \\ \vdots & \vdots & \ddots & \vdots & \ddots & \vdots \\ \frac{\partial P_{C[nx-1][ny-1][nt-1]}}{\partial P_{I[0][0][0]}} & \frac{\partial P_{C[nx-1][ny-1][nt-1]}}{\partial P_{I[0][0][1]}} & \cdots & \frac{\partial P_{C[nx-1][ny-1][nt-1]}}{\partial P_{I[0][0][nz-1]}} & \cdots & \frac{\partial P_{C[nx-1][ny-1][nt-1]}}{\partial P_{I[nx-1][ny-1][nz-1]}} \end{bmatrix} \tag{2}$$

$$\mathbf{P_I} = \begin{bmatrix} P_{I[0][0][0]} \\ P_{I[0][0][1]} \\ \vdots \\ P_{I[0][0][nz-1]} \\ \vdots \\ P_{I[nx-1][ny-1][nz-1]} \end{bmatrix}, \quad \mathbf{P_M} = \begin{bmatrix} P_{M[0][0][0]} \\ P_{M[0][0][1]} \\ \vdots \\ P_{M[0][0][nt-1]} \\ \vdots \\ P_{M[nx-1][ny-1][nt-1]} \end{bmatrix} \tag{3}$$

where, $\mathbf{P_I}$ is the source distribution of sound waves to be estimated, $\mathbf{P_M}$ is the distribution of measured data which are arranged in the spatiotemporal space, and $\mathbf{J}$ is a Jacobian matrix which gives all correspondences between unit sources and signals of sound waves generated by these sources.

In order to get signals of photoacoustic waves, we compute the accurate forward photoacoustic models which incorporate the system-configuration and detector-dependent factors such as frequency response and finite-size effect. In this work, we integrate Green's function to calculate the forward models. The effects of refraction due to the holding plate are corrected on the basis of Snell's law.

We assume that the probability distribution of measured data is a Gaussian distribution:

$$p(y) = \frac{1}{\sqrt{2\pi\sigma^2}} e^{-(y-\mu)^2/2\sigma^2} \tag{4}$$

In Eq. (4), μ is the average value of all measured data, and σ is the variance of these data.

In this assumption, maximum likelihood estimation of measured data that maximizes the likelihood (Eq. (5)) is equivalent to the least-squares method which solves the normal equation.

$$p(y_1, y_2, \cdots, y_N) = \prod_{\alpha=1}^{N} \frac{1}{\sqrt{2\pi\sigma^2}} e^{-(y_\alpha - f(x_\alpha))^2/2\sigma^2} \tag{5}$$

In Eq. (5), x represents an unknown, and $f(x)$ is the relation between measured data and the unknown in case of no error.

We introduce an objective function (Eq. (6)) which consists of the residual between the measured acoustic signals and the signals predicted by the forward models and the regularization term, and solve the regularized normal equation (Eq. (7)) to minimize the objective function.

$$F = \frac{1}{2}\left\|\mathbf{J}\mathbf{P_I} - \mathbf{P_M}\right\|^2 + \frac{1}{2}\lambda\left\|\mathbf{P_I}\right\|^2 \tag{6}$$

$$\left(\mathbf{J}^{\mathrm{T}}\mathbf{J} + \lambda\mathbf{I}\right)\mathbf{P_I} = \mathbf{J}^{\mathrm{T}}\mathbf{P_M} \tag{7}$$

The regularization term included in Eq. (6) stabilizes the conditioning of the problem. λ is the regularization parameter. In order to minimize the objective function, we apply the diagonally scaled conjugate gradient (CG) method for optimization and obtain the optimal solution.

2.3 Memory reduction and speed up of the calculation

Generally, the Jacobian matrix $\mathbf{J}$ is so huge in three-dimensional problems that not all elements of $\mathbf{J}$ can be held in memory at the same time. However, we can reduce the elements of $\mathbf{J}$ in memory because photoacoustic waves have translational symmetry in a planar system: we have only to hold $\mathbf{J_{min}}$ (Eq. (8)) in memory, which is the minimal set of $\mathbf{J}$, and refer to the corresponding elements cyclically.

$$\mathbf{J}_{\min} = \left[\mathbf{j}_{[0][0][0]}, \mathbf{j}_{[0][0][1]}, \cdots, \mathbf{j}_{[0][0][nz-1]}\right]$$

$$\mathbf{j}_{[i][j][k]} = \begin{bmatrix} \dfrac{\partial P_{C[0][0][0]}}{\partial P_{I[i][j][k]}} \\ \dfrac{\partial P_{C[0][0][1]}}{\partial P_{I[i][j][k]}} \\ \vdots \\ \dfrac{\partial P_{C[0][0][nt-1]}}{\partial P_{I[i][j][k]}} \\ \vdots \\ \dfrac{\partial P_{C[nx-1][ny-1][nt-1]}}{\partial P_{I[i][j][k]}} \end{bmatrix} \tag{8}$$

Furthermore, each **j** matrix can be compressed into the band matrix because of the sparseness of the matrix owing to the locality of photoacoustic waves. The original addresses of the compressed band matrix elements are stored simultaneously. We have only to refer to the band matrix elements with the original addresses, and hence the computational time is reduced to approximately one tenth.

3. SIMULATION RESULTS

In this section we present simulation results of our reconstruction algorithm. The simulated geometry is shown in Fig. 1(a), where a cubic region (32 mm in each dimension, speed of sound = 1500 m/s) contains three spherical sources with a radius of 0.5 mm. These spherical sources are located at 8 mm, 16 mm, 24 mm from the bottom, respectively. There is a holding plate on the bottom of the cubic region (10 mm in thickness, speed of sound = 2200 m/s). The transducer array (64×64 elements in each dimension) is on the bottom of the holding plate. The mesh used for the simulations had $64 \times 64 \times 64$ elements. The measured data were generated using accurate forward photoacoustic models which incorporate the system-configuration and detector-dependent factors. The dimensions of the measured data were 64×64 elements in the space domain and 512 elements in the time domain. The cost of each iteration of the CG method was approximately 8 minutes on a 3.2-GHz Xeon 5400 PC with 16 GB of memory.

Figure 2(a) and 2(b) show three-dimensional volume rendering images of reconstructed data: 2(a) is an image which was reconstructed by our proposed model-based reconstruction algorithm, and 2(b) was reconstructed by the universal back-projection algorithm (UBP) with correction of the holding plate. Figure 2 shows that the image reconstructed by the UBP algorithm suffers from the limited view effect which degrades the lateral resolution and the detector-related blur effect. On the other hand, the image reconstructed by our model-based algorithm does not suffer from these effects, and the lateral resolution is homogeneous in the whole region.

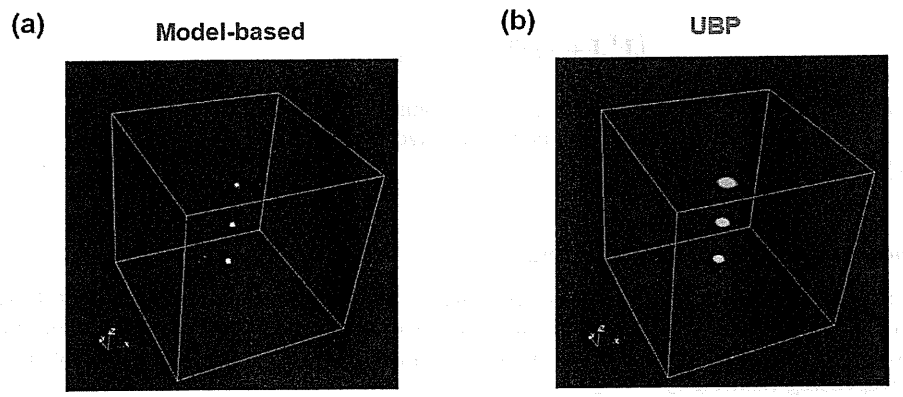

Figure 2. Reconstructed images: (a) Model-based, (b) UBP.

Figure 3(a) shows the cross-sectional 2D images reconstructed by both algorithms. Figure 3(b) shows the cross-sectional profile at the upper spherical source. As these figures show, the lateral resolution is significantly improved by our proposed model-based algorithm.

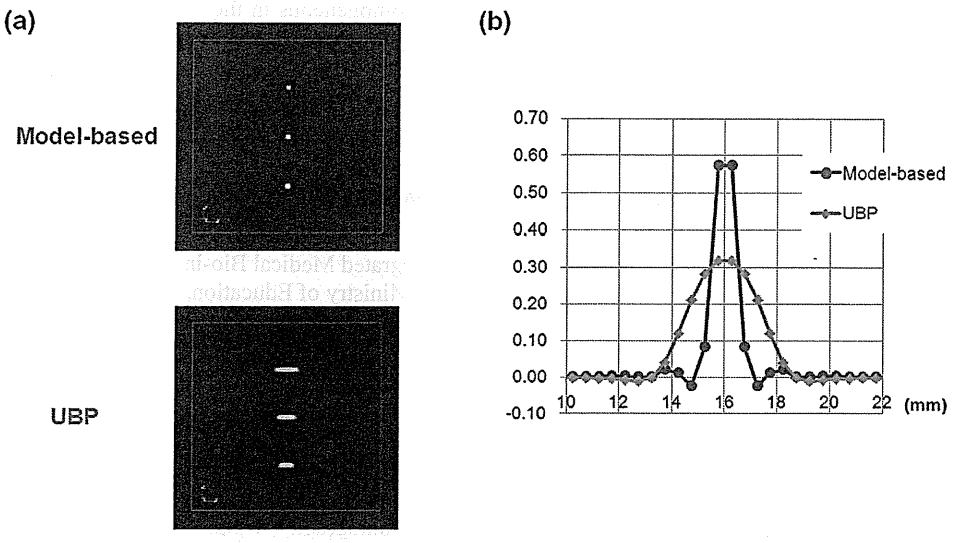

Figure 3. (a) Cross-sectional 2D images, (b) cross-sectional profile at the upper spherical source.

Figure 4 shows the relation between the transducer size and the lateral resolution. As shown, although the lateral resolution is improved by using a smaller transducer, the UBP algorithm cannot reach the upper limit of the lateral resolution (which is equivalent to the diameter of the spherical source) due to the limited view condition. On the other hand, the model-based algorithm can reach the upper limit of the resolution more effectively by the use of a smaller transducer.

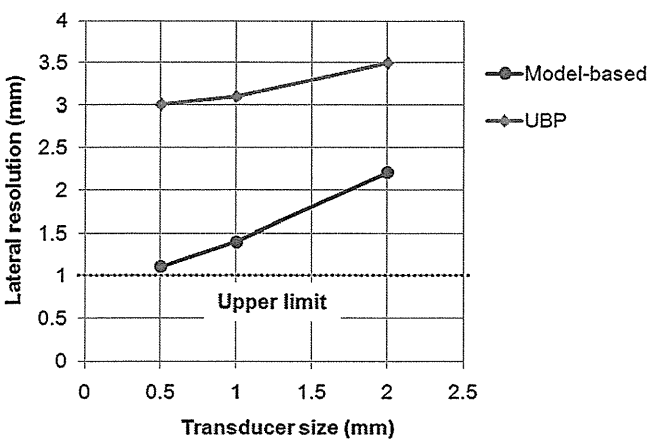

Figure 4. Lateral resolution vs. transducer size (Model-based and UBP).

4. CONCLUSIONS

We explored the possible application of a three-dimensional model-based reconstruction algorithm in the time domain. The use of the symmetry and locality of photoacoustic waves reduces the memory requirements and computation time in three-dimensional image reconstruction. Compared with the UBP algorithm, three-dimensional simulation results indicate that our algorithm improves the lateral resolution, which is homogeneous in the whole region. In addition, the images reconstructed by our method do not suffer from system-configuration and detector-related effects, which is useful in our developed PAT system with limited view condition.

In a future work, we will evaluate our method using experimental data and examine its application to larger systems.

ACKNOWLEDGEMENT

This work was partly supported by the Innovative Techno-Hub for Integrated Medical Bio-imaging Project of the Special Coordination Funds for Promoting Science and Technology, from the Ministry of Education, Culture, Sports, Science and Technology (MEXT), Japan.

REFERENCES

[1] Minghua Xu and Lihong V. Wang, "Universal back-projection algorithm for photoacoustic computed tomography" Phys. Rev. E 71, 016706 (2005).

[2] DaB. T. Cox, S. R. Arridge, and P. C. Beard, "Photoacoustic tomography with a limited-aperture planar sensor and a reverberant cavity" Inv. Prob. 23, 95-112 (2007) .

[3] Huabei Jiang, Zhen Yuan, and Xuejun Gu, "Spatially varying optical and acoustic property reconstruction using finite-element-based photoacoustic tomography" J. Opt. Soc. Am. A 23(4), 878-888 (2006).

[4] Zhen Yuan and Huabei Jiang, "Three-dimensional finite-element-based photoacoustic tomography: Reconstruction algorithm and simulations" Med. Phys. 34(2), 538-546 (2007).

[5] Lei Yao and Huabei Jiang, "Finite-element-based photoacoustic tomography in time domain" J. Opt. A: Pure Appl. Opt. 11, 085301 (2009).

[6] K. Fukutani, Y. Someda, M. Taku, Y. Asao, S. Kobayashi, T. Yagi, M. Yamakawa, T. Shiina, T. Sugie, and M. Toi, "Characterization of photoacoustic tomography system with dual illumination modes," Proc. SPIE 7899 (2011).

Digestive Endoscopy
Journal for Gastroenterologists and Endoscopic Surgeons

Digestive Endoscopy (2010) **22**, 259–267 doi:10.1111/j.1443-1661.2010.01010.x

REVIEW

ANGIOGENESIS IN SUPERFICIAL ESOPHAGEAL SQUAMOUS CELL CARCINOMA: MAGNIFYING ENDOSCOPIC OBSERVATION AND MOLECULAR ANALYSIS

YOUICHI KUMAGAI,[1] MASAKAZU TOI,[2] KENRO KAWADA[3] AND TATSUYUKI KAWANO[3]

[1]*Department of Surgery, Ohta Nishinouchi Hospital, Fukushima,* [2]*Department of Surgery, Kyoto University, Kyoto and* [3]*Department of Surgery, Tokyo Medical and Dental University, Tokyo, Japan*

Observations of esophageal squamous cell carcinoma using magnifying endoscopy have now been carried out extensively and, as a result, it has become clear that the morphology of the microvessels evident at the tumor surface reflects the depth of tumor invasion. In M1 and M2 cancer, the surface microvasculature reveals dilation and elongation of the intrapapillary capillary loops (IPCL). However, at this stage, some immature capillaries resembling IPCL also arise inside the tumor and, therefore, the view of the microvasculature should be described as one showing 'intermixing of modified IPCL and IPCL-like immature capillaries (IPCL-like abnormal capillary)'. As cancer invades into the muscularis mucosa (M3 or deeper), an obviously dilated and irregularly branched tumor-specific vasculature, more accurately described as 'neovasculature', can be observed. From our magnifying endoscopy observations and studies of the molecular profile of early esophageal cancer, we conclude that two major angiogenic steps exist in precancerous and M3 lesions in the early phase of cancer progression. In addition, it is now possible to study cell morphology using an endocytoscope with a much higher magnification (×400–×1000) than magnifying endoscopes currently on the market. The histology revealed in this way may reduce the need for conventional biopsy histology in the future.

Key words: angiogenesis, endocytoscopy system, esophageal cancer, magnifying endoscopy, squamous cell carcinoma, virtual histology.

INTRODUCTION

The most important strategy for successful cure of esophageal cancer is detection at an early stage of cancer progression. Such early-stage cancers are considered to be curable by endoscopic mucosal resection (EMR), which is only minimally invasive, and the resulting clinical prognosis is good. (In the present review, the depth of invasion of superficial esophageal carcinoma is given in accordance with the subclassification criteria of the Japan Esophageal Society [Guidelines for Esophageal Cancer Treatment].[1])

EMR or endoscopic submucosal dissection (ESD) is unequivocally indicated for the treatment of carcinoma in situ (M1) and tumor invasion to the lamina propria mucosa (M2) esophageal squamous cell carcinoma (ESCC), and it may also be applicable to tumor invasion to the muscularis mucosa (M3) and tumor invasion to the upper third of the submucosal layer (SM1) cancer, depending on whether lymph node metastasis is present.[2] However, advanced esophageal cancers require radical surgery that leads to a deterioration in the quality of life and is associated with a poorer prognosis.[3,4]

Recently, magnifying observation at up to ×80 with narrow-band imaging has proved to be effective for detecting early-stage ESCC.[5–8] Furthermore, the morphology of the surface microvessels of a tumor is known to reflect the depth of tumor invasion. Such diagnosis is based on observations of angiogenesis during cancer progression.[9] The esophagus is the only organ for which morphological change from a normal microvasculature to that characterizing early-stage or advanced cancer has been demonstrated using magnifying endoscopy. To understand this phenomenon, it is important not only to elucidate the process of angiogenesis in the early phase of cancer progression, but also to consider molecular targeting therapy or chemoprevention.

In the present review, we report the current state of progress of magnifying observation of ESCC, focusing on the morphology of the surface microvasculature, and the correlation between these endoscopic findings and the molecular features reported in the literature.

SEARCH STRATEGY AND SELECTION CRITERIA

Published and unpublished data for this review were identified by searches of PubMed, US National Library of Medicine, National Institute of Health (http://www.ncbi.nlm.nih.gov/pubmed/) and references from relevant articles. We have also cited some articles from our own database.

Search Terms Included: 'magnifying endoscopy', 'esophageal cancer', 'squamous cell carcinoma', 'endocytoscopy',

Correspondence: Youichi Kumagai, Department of Surgery, Ohta Nishinouchi Hospital, Nishinouchi 2-5-20, Kohriyama-shi, Fukushima 963-8558, Japan. Email: kuma7@ohta-hp.or.jp

Received 9 April 2010; accepted 7 June 2010.

'angiogenesis', 'apoptosis', 'chemokine', 'cyclooxygenase', 'cytokine', 'hypoxia', 'NO', 'oncogene', 'VEGF', 'PD-ECGF (TP)', 'bFGF', 'HER2' and 'p53'.

BACKGROUND TO THE DEVELOPMENT OF MAGNIFYING ENDOSCOPY FOR OBSERVATION OF THE ESOPHAGUS

Magnifying observation of the esophageal mucosa was first reported by Kozu *et al.* in 1975.[10] They used a ×25 magnifying endoscope to study various esophageal lesions. However, because of the prevailing clinical circumstances at the time, all of the cases they studied were advanced squamous cell carcinomas. In 1991, Makuuchi *et al.* reported magnifying observation of the surface microvasculature of superficial esophageal carcinoma.[11] However, that study used a relatively low-powered magnifying endoscope, and its clinical applicability was therefore limited. Magnifying endoscopic observation of the normal esophageal mucosa and ESCC using the GIF-200UHM (Olympus medical Systems Co. Tokyo, Japan), which had a magnifying capacity of ×150, was first reported by Inoue *et al.*,[5,6] who succeeded in discovering looped capillary vessels inside the epithelial papillae (intrapapillary capillary loops [IPCL]). The IPCL inside cancer lesions were demonstrated to show abnormal changes, such as 'dilation, weaving, changes in caliber, and variety of shape'. It also revealed that the morphology of the surface vasculature of superficial esophageal cancers exhibited characteristic changes according to the depth of tumor invasion. However, the area observed by magnifying endoscopy was narrow (approximately 3 × 3 mm) and, thus, there was some concern as to whether the microvasculature that was demonstrated matched the findings of histological observations. In addition, it was considerably disadvantageous that the microvasculature could not be observed in the resected esophagectomy specimens, in view of their lack of pooled blood. To solve this problem, Kumagai *et al.* introduced MICROFIL (Flow Tech, Inc., Carver, MA, USA), which was injected to fill the microvessels of the resected specimen. Comparison of the normal esophageal mucosa and cancer lesions injected with MICROFIL using a stereoscopic microscope confirmed the validity of magnifying observation.[7] During the same period, Arima *et al.* reported that the vessels present at the surface of the esophageal mucosa showed characteristic changes according to the degree of atypia or depth of cancer invasion.[12,13] Thereafter, with an increase in cases observed by magnifying endoscopy, each of the two groups proposed different classifications (Inoue classification and Arima classification), which has resulted in the use of two standards at the present time in Japan.

In 2009, Olympus Medical Systems Co. (Tokyo, Japan) manufactured a novel magnifying endoscope, the GIF-Y0002, that has a single lens for which the magnification can be consecutively increased from the conventional endoscopy level to ×380.[14,15] The GIF-Y0002 is designed to allow observation of the surface cells (i.e. as an endocytoscope), as well as visualizing the surface vasculature at higher power, also allowing observation of blood flow in the surface vessels in some cases.

TECHNIQUE OF OBSERVATION USING MAGNIFYING ENDOSCOPY AND ITS RESULTS FOR ESCC

The preparations for magnifying observation, including pharyngeal anesthesia, are similar to those for conventional endoscopy. Sometimes, however, it is difficult to obtain detailed pictures because of mucosal movement caused by heartbeat, respiration and peristalsis. Therefore, we have devised some methods for limiting such technical failure. First, a soft plastic hood 2-mm thick is attached to the distal end of the magnifying endoscope to maintain an appropriate distance from the target tissue and to allow observation at the maximum magnification of ×80. We have also tried to exclude the influence of peristalsis and swallowing by using i.v. midazolam and i.m. scopolamine butylbromide.[7,16,17]

Magnifying observation of ESCC is useful for pretreatment diagnosis of depth of tumor invasion. Based on a study of 263 esophageal cancers, Arima *et al.* reported that the diagnostic accuracy of magnifying endoscopy for depth of invasion was 98.8% for M1 and M2 cancers, 68% for M3 and SM1 cancers, and 84.0% for tumor invasion to the middle third (SM2) and lower third (SM3) of the submucosal layer cancers.[12,13] They concluded that magnifying observation facilitated the identification of lesion microinvasion, thereby increasing the proportion of correctly diagnosed M3 or SM1 cancers in comparison with conventional endoscopic diagnosis.

Kumagai *et al.* also reported that the rate of accurate diagnosis of depth of invasion was 83.3% in cases where detailed pictures were obtainable using magnifying endoscopy. They mentioned that it was possible to clearly distinguish the depth of invasion of the tumor as shallower than M2 or deeper than M3, considering the superficial microvasculature of the esophageal cancer.[7,17]

MICROVASCULAR ARCHITECTURE OF THE NORMAL ESOPHAGEAL MUCOSA

Several groups have described the microvascular architecture of the normal esophageal mucosa, in relation to analysis of esophageal varices.[18–20] Aharinejad *et al.*[21] reported a detailed three-dimensional analysis of the esophageal microvasculature based on a study of microvascular corrosion casts of the esophagus using scanning electron microscopy. They noted the IPCL as 'capillary loops protruding towards the lumen' in observations of guinea-pigs and rats. However, they did not mention the presence of these capillary loops inside the epithelial papillae.

Based on observations in humans using ×120 magnifying endoscopy, Inoue *et al.* reported that submucosal vessels connected to the arborescent vascular network could be observed at lower magnification. These arborescent vessels are recognizable as being interconnected, usually at the level of the fourth branch of the fine network. At higher magnification, capillary vessels in the papillae after the arborescent vessels can be observed. Furthermore, every intrapapillary capillary was observed as a single capillary loop. These were referred to as 'intrapapillary capillary loops' (IPCL).[5] (Fig. 1a).

Kumagai *et al.* clarified the relationship between this vascular structure and the esophageal wall using stereoscopic

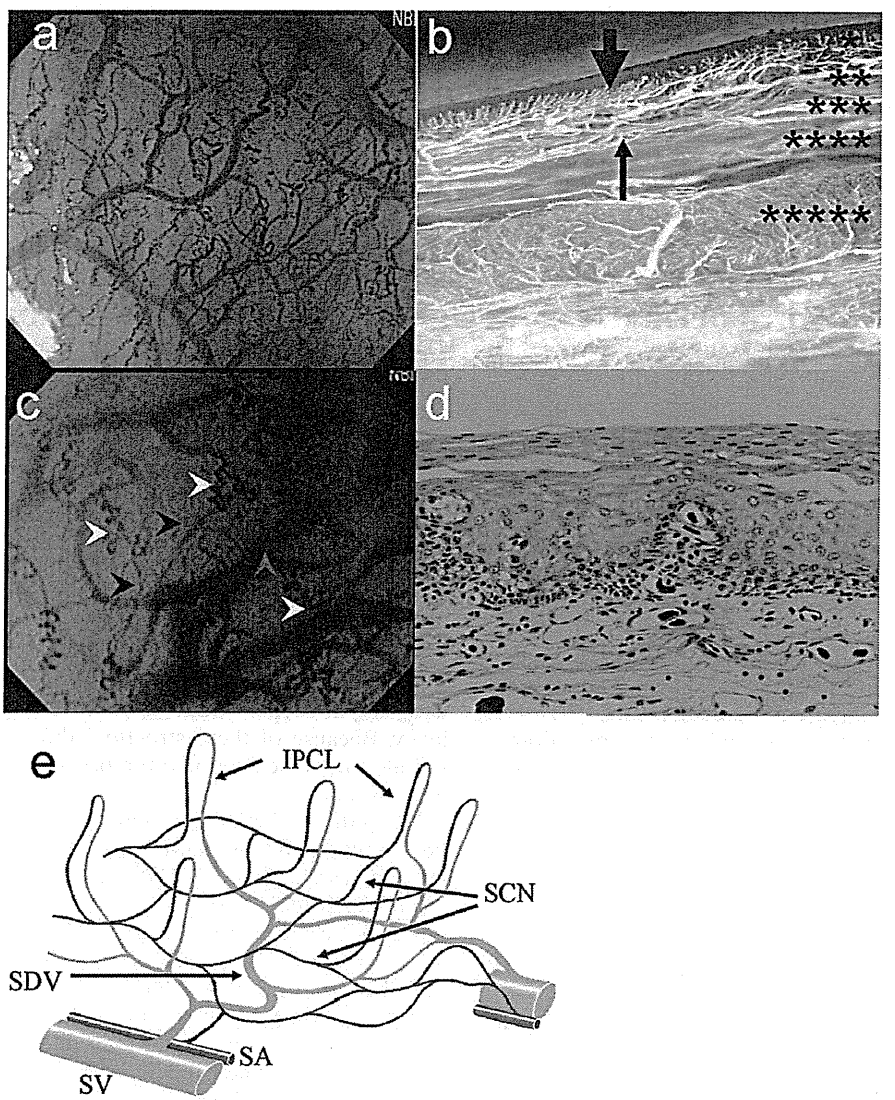

Fig. 1. (a) Normal squamous epithelium observed by magnifying endoscopy at ×80 (narrow band imaging). Arborescent vascular network and normal intrapapillary capillary loops (IPCL) are evident. (b) Cross-section of the esophageal wall after injection of MICROFIL (Flow Tech, Inc., Carver, MA, USA). The relationship between the arborescent vascular network and IPCL is clearly visualized. *, squamous epithelium; **, lamina mucosal propria; ***, muscularis mucosae; ****, submucosa; *****, muscularis propria. Small arrow, aborescent vascular network; large arrow, IPCL at the surface of the mucosa. (This figure is quoted from ref. no. 7.) (c) Microvasculature of the normal esophageal mucosa using the highest magnification of the GIF-Y0002 (Olympus Medical Systems Co., Tokyo, Japan) (narrow band imaging). We were able to visualize the relationship between the subepithelial capillary network of the arterioles, IPCL and subepithelial drainage venules. Black arrow, subepithelial capillary network of the arterioles; white arrow, IPCL; red arrow, subepithelial drainage venules. (This figure is quoted from ref. no. 15.) (d) Histological section of the normal esophageal wall after MICROFIL injection. Epithelial papillae and IPCL are evident. (e) Schema of the superficial vascular network of the normal esophageal mucosa. SA, submucosal artery; SCN, subepithelial capillary network; SDV, subepithelial drainage vein; SV, submucosal vein. (This figure is quoted from ref. no. 15.)

microscopy after MICROFIL injection.[7] They mentioned that the vessels pierced the muscle layer, forming an arborescent vascular network. This network was relatively sparse in the submucosal layer, but became dense both above and below the muscularis mucosae. In addition, these arborescent vessels gradually formed a thin net as they rose to the surface of the esophageal mucosa, and finally formed the IPCL (Fig. 1b). Furthermore, the IPCL were arranged regularly at intervals of approximately 100 μm, which corresponds to the maximum distance oxygen can diffuse from a vessel.[7,9]

Use of the GIF-Y0002 has made it possible to clearly distinguish arterioles and venules based on observation of blood flow. We were able to visualize the relationship between the subepithelial capillary network of the arterioles, IPCL, and subepithelial drainage venules. The arterioles arising in the lamina propria mucosae formed a subepithelial capillary